Chandra Confirmation of a Pulsar Wind Nebula in DA 495

Z. Arzoumanian[1,2]

zaven@milkyway.gsfc.nasa.gov

S. Safi-Harb[3]

T. L. Landecker[4]

R. Kothes[4,5]

and

F. Camilo[6]

Received _____; accepted _____

[1]CRESST and X-ray Astrophysics Laboratory, NASA-GSFC, Greenbelt, MD 20771.

[2]Universities Space Research Association, Columbia, MD 21044.

[3]Department of Physics and Astronomy, University of Manitoba, Winnipeg, MB, R3T 2N2, Canada.

[4]National Research Council of Canada, Hertzberg Institute of Astrophysics, Dominion Radio Astrophysical Observatory, Penticton, British Columbia, V2A 6J9, Canada.

[5]Department of Physics and Astronomy, University of Calgary, Calgary, AB, Canada.

[6]Columbia Astrophysics Laboratory, Columbia University, New York, NY 10027.

Abstract

As part of a multiwavelength study of the unusual radio supernova remnant DA 495, we present observations made with the *Chandra X-ray Observatory*. Imaging and spectroscopic analysis confirms the previously detected X-ray source at the heart of the annular radio nebula, establishing the radiative properties of two key emission components: a soft unresolved source with a blackbody temperature of 1 MK consistent with a neutron star, surrounded by a nonthermal nebula 40″ in diameter exhibiting a power-law spectrum with photon index $\Gamma = 1.63$, typical of a pulsar wind nebula. Morphologically, the nebula appears to be slightly extended along a direction, in projection on the sky, previously demonstrated to be of significance in radio and *ASCA* observations; we argue that this represents the orientation of the pulsar spin axis. At smaller scales, a narrow X-ray feature is seen extending out 5″ from the point source, but energetic arguments suggest that it is not the resolved termination shock of the pulsar wind against the ambient medium. Finally, we argue based on synchrotron lifetimes in the nebular magnetic field that DA 495 represents the first example of a pulsar wind nebula in which electromagnetic flux makes up a significant part, together with particle flux, of the neutron star's wind.

Subject headings: ISM: individual (DA 495, G65.7+1.2) — radiation mechanisms: nonthermal — stars: neutron — supernova remnants — X-rays: ISM

the physical mechanisms of energy transfer, the local conditions (particle densities, flow velocities, magnetic field strengths, etc.), and the nature of the particle-accelerating central engine.

Although its identification as a pulsar-powered SNR is now virtually certain, no object in this class quite resembles the radio nebula DA 495 (Landecker & Caswell 1983): the morphology is distinctly annular, with a radial profile that rises rapidly from a central emission deficit (the "hole") then falls gradually with increasing distance from the center (see Fig. 1 for a contour map, and Kothes et al. 2007 for a detailed discussion of the radio properties). We described in an earlier paper (Arzoumanian et al. 2004; hereafter, ASLK04) X-ray observations of DA 495 that revealed the central engine powering the radio nebula, the *ROSAT* source 1WGA J1952.2+2925, and provided some evidence for extended X-ray emission consistent with a PWN. To confirm the existence of a high-energy nebula, and because lingering doubts remained about a possible "thick shell" thermal origin for the annulus (Velusamy et al. 1989), we set out to perform with *Chandra* an X-ray observation sensitive to compact nonthermal structures as a means of strengthening the identification of DA 495 as a PWN. The detection in particular of jets, toroidal structures, or other markers of large-scale axial symmetry, such as those seen in the Crab, Vela, and similar pulsars, would provide strong evidence for the identification of DA 495 as a pulsar-powered supernova remnant.

2. Observations

The *Chandra* observation of DA 495 was carried out on 2002 December 9. Anticipating the need for a large field of view—to search for X-ray emission from the entire $\sim 20'$-diameter radio nebula—we used the Advanced CCD Imaging Spectrometer (ACIS) instrument with the putative pulsar, 1WGA J1952.2+2925 (see ASLK04), placed at the aimpoint of the I3

1. Introduction

With the *Chandra X-ray Observatory*'s first glimpse of the Crab pulsar (Weisskopf et al. 2000), a new window was opened onto the interactions of neutron stars with their surroundings. Rotation-powered pulsars drive outflows of particles and electromagnetic energy into the immediate environment; depending primarily on the pulsar's age, this environment might simply be the interstellar medium or, in the case of young, energetic pulsars, the circumstellar debris of the supernova explosion that created the neutron star. The astrophysical value of these interactions lies in their uniqueness as a probe of the content of pulsar winds, which originate in the incompletely understood magnetospheres of neutron stars, and of the physics of particle acceleration and shock mixing of relativistic and non-relativistic fluids. In contrast to the optical and radio observations that provided early insights into these phenomena, X-ray studies, in particular with *Chandra*'s unequalled angular resolution, sample the properties of energetic and short-lived particles nearest the accelerating engines that produce them.

In the class of filled-center supernova remnants (SNRs), the bulk of the radiation from a remnant can be traced back energetically to the rapidly rotating neutron star at its core, with emission from the shocked neutron star wind often defining a pulsar wind nebula (PWN). Shell-type remnants, by contrast, expend the energy of the supernova explosion's blast wave. Evidence for the transfer of a neutron star's rotational kinetic energy to its surroundings is provided by the axisymmetric structures—arcs, rings, tori, and jets—seen in high-resolution X-ray images of a variety of pulsars. Together with amorphous nonthermal emission also found around energetic pulsars, these structures result from synchrotron radiation by the pulsar's ultrarelativistic particle wind where it is confined and perturbed by the surrounding medium; see, e.g., Gaensler & Slane (2006) for a review of PWNs. The morphological and spectral properties of PWNs carry valuable information about

CCD. The 4-chip ACIS-I array neatly captured most of the radio extent of DA 495 within its 16.9′ square field of view. Two additional CCDs, the front-illuminated chips ACIS-S2 and -S4 were also activated to provide a measure of the X-ray background in fields adjacent to the radio nebula; ultimately, S4 was not used because it suffered from excess instrument noise difficult to distinguish from cosmic background.

X-ray photon events were acquired in timed-exposure (TE) readouts of the ACIS CCDs, and telemetered to the ground in Very Faint mode. The starting points for our analyses were event lists, aspect solutions, and other standard data products resulting from the third reprocessing (REPRO-III) of raw data at the *Chandra* X-ray Center. We used the CIAO software package (version 3.3.0.1; Fruscione et al. 2006) and associated calibration database (CalDB version 3.2.3) for reduction of the ACIS data.

3. Results

Following standard data preparation procedures[1] for filtering (e.g., rejection of events due to particle background rather than cosmic X-rays), effective area and energy calibrations, and mapping of detector to sky coordinates, final ACIS photon event lists were used to cumulate images, spectra, and lightcurves for further analysis. For an observation duration of 25,160 s, a total filtered exposure of 24,843 s was acquired. We found that photon events outside the 0.6–7 keV energy band were consistent with background and provided little useful information; unless noted otherwise, all of the following discussion refers to analysis and results in this energy range.

---

[1]Standard procedures are described in CIAO software analysis guides and "threads" available at `http://cxc.harvard.edu/ciao/guides/`.

3.1. Image Analysis

The map of X-ray counts on the sky for all CCDs active during the 25 ks *Chandra* observation, binned by a factor of 16, is shown in Figure 1, with radio contours superposed. The basic result of earlier *ROSAT* and *ASCA* observations (ASLK04), that an X-ray source lies near the center of the DA 495 annulus, is readily upheld (source 'A'). ASLK04 argued further that the *ASCA* images were consistent with a blend of soft emission from a compact source and harder emission from a nebula barely resolved by the available $\sim 1'$ angular resolution. This statistically less-robust conclusion is unambiguously confirmed, as discussed below, with the leap to *Chandra*'s arcsecond-level imaging capability.

To allow for morphological analysis with the best available angular resolution, we formed ACIS images with pixel randomization (used by default in standard CIAO data reduction to avoid spatial digitization effects) disabled; we also applied the sub-pixel event localization algorithm described by Mori et al. (2001). In practice, we found that these techniques produced no discernible change in the morphology of the diffuse X-ray emission, but yielded a somewhat improved ($\sim$ 10%) concentration of counts onto the point-like source from its immediate vicinity. The coordinates of the unresolved source on the sky are (J2000) RA $19^{\rm h}52^{\rm m}17\overset{\rm s}{.}04$, Dec $+29°25'52\overset{''}{.}5$, good to the nominal *Chandra* astrometric uncertainty of $0.6''$.

In the full-resolution ACIS-I image, Figure 2, the X-ray nebulosity is revealed to be $\sim 40''$ in diameter. The extended emission surrounds the point-like source but is not centered on it. Instead, there is a strong asymmetry, roughly along an east-west line, in both flux and radial extent, with most of the diffuse flux lying to the east of the unresolved source. To quantify this asymmetry, we sum the counts detected within the eastern and western halves of a $20''$-radius circle centered on the point source, neglecting the latter's flux by excluding the central $2''$-radius circle. Of the 474 counts that define the X-ray

nebula and are contained within the larger circle, 314 lie to the east and 160 to the west of the north-south bisector. As shown in Figure 2, we choose an extraction region for spectral analysis that is not centered on the point source, in order to better match the asymmetric shape of the nebula. The background-subtracted countrate within this extraction circle was 18.4 ± 1.5 cts ks^{-1}. For the unresolved source, 175 counts were detected in a 2″-radius region centered midway between the two brightest pixels, for a background-subtracted countrate of 7.0 ± 1.3 cts ks^{-1}; the same region was used to accumulate a spectrum. Figure 2 displays the *Chandra* data in two energy bands, smoothed and unsmoothed; the softness of the point source relative to the extended emission is evident.

The low surface brightness of the X-ray nebulosity (0.36 cts arcsec^{-2}) and the brevity of the observation conspire to make difficult the identification of any well-defined structures within the nebula. Smoothing of a raw counts image can increase the significance of faint features if their extents are well-matched to the smoothing scale, but the resulting images can also be misleading if over-interpreted. Nevertheless, we experimented with various smoothing techniques to attempt to discern compact structures such as those exemplified by the Crab nebula. Two candidate features emerge. The first is an apparent arc of emission, resembling an inverted hook, just 10 pixels (4.92″) in extent and immediately adjacent to the point source: it extends initially to the east and then curves south (Fig. 3). Whether this feature is truly curved is unclear, but it is sufficiently bright in the unsmoothed image (61 counts in a 15×9-pixel elliptical extraction region) relative to the local background (an average of 21 counts in with the same elliptical region positioned at four nearby locations) that it is statistically significant at the 4σ level. The apparent curvature results from a deficit of counts immediately to the SE of the point source, but statistical fluctuations could account for this deficit.

The second structural detail suggested by the data, near the detection limit for low

surface-brightness features, is slightly enhanced flux along a line (labeled "NE Extension" in Fig. 3) extending from the point source to the northeast. In Figure 3, we plot the counts contained within a number of identical rectangular strips, centered on the point source and rotated at 10° intervals. The resulting measurements are found to be roughly consistent with a constant flux, but although the deviations from the mean are not highly significant, the trend is suggestive of an enhancement along the line at 50° north through east. Consistent with the overall east-west asymmetry in the nebular flux, the elongated emission that may exist to the northeast is clearly nonexistent in the opposite direction, to the southwest of the point source; repeating the counting analysis shown in Figure 3 with a rectangular region that only samples the semicircular region to the east of the point source (out to the same radius) results in a statistically more significant peak at 50°.

While the evidence for this elongation in the *Chandra* data alone is unconvincing, two other measurements lend support to make it more compelling (cf. Fig. 3). First, in the work of Kothes et al. (2007; hereafter, KLR+07), multi-frequency radio polarization studies of DA 495 allow for the measurement of its spatially-varying rotation measure. Combined with modeling of the particle densities within the remnant, the orientation of the intrinsic magnetic field can be derived. The result favors a dipolar field oriented at 50°, identically to the *Chandra* elongation, in projection on the sky. Second, in our analysis of *ASCA* data (ASLK04) we argued—without prior knowledge of the radio nor *Chandra* results—that the marginally resolved hard source was extended along a NE-SW direction. Figure 3 overlays the innermost *ASCA*-GIS smoothed-intensity contour onto the *Chandra* image. Although its 1-arcmin angular resolution is substantially worse than *Chandra*'s, the two *ASCA*-GIS instruments taken together provide sensitivity (in terms of effective area) comparable to the ACIS-I camera at energies above ~ 3 keV; moreover, the convolution of a $\sim 40''$ nebula with a $\lesssim 1'$ point-spread function should result in a measurably extended feature, so it is perhaps not surprising that the results from the two telescopes are consistent in the orientation of

the elongation.

Finally, we note with interest that the two diffuse features, the hook and the elongation, appear to lie in orthogonal directions, suggestive of equatorial and polar structures seen in many PWNs. We discuss this possibility further below.

Aside from the unresolved and diffuse X-ray emission believed to be associated with DA 495, forty-eight additional sources are seen in the ACIS-I field of view. Notable ones include (cf. Figs. 1 and 2):

CXOU J195217.1+292532, a faint (ten counts in a 3×3-pixel area), hard, unresolved source, 21″ south of source A. Visible in the hard-band images in Figure 2, this object is unlikely to be related to DA495, and is probably extragalactic. No counterpart at another wavelength has been cataloged.

CXOU J195253.1+292633 (Source B), the X-ray counterpart of a Guide Star Catalog star (N2FA105281) that lies 13′ from the telescope axis; at this position, the mirror point-spread function is far from ideal, giving the star a distended appearance. Nevertheless, 450 counts were collected from this soft source.

CXOU J195217.4+292745 (Source C), coincident with an unresolved feature in radio images and consisting of nine counts in a 3×3-pixel area, all between 2 and 8 keV. We believe that source C is also extragalactic, presumably a background AGN that may be better distinguished from DA 495 in higher-resolution radio images. No counterpart at another wavelength has been cataloged.

3.2. Spectral Analysis

Spectral analysis was carried out for three source regions: the point source at the heart of DA 495, the surrounding diffuse emission out to a radius of 20″, and a larger annulus encompassing the brightest parts of the radio nebula to search for thermal X-ray emission associated with a "thick shell" supernova remnant. Suitable background regions, in some cases more than one, were identified for each source region; serendipitous sources were excised and background spectra subtracted from accumulated source spectra prior to fitting with the `Sherpa` software.

Following the results of KLR+07, we adopt an assumed distance to DA 495 of 1 kpc in estimating luminosities of the various emission components.

3.2.1. Nebula and Point Source

Point-source and nebular spectra were formed using the `psextract` and `specextract` scripts, respectively, with response matrices for the regions of interest generated using the `mkacisrmf` tool. For the point source, a circular extraction region with a radius of 4 pixels ($\sim 2''$), centered midway between the two brightest pixels, was defined and events were grouped in energy so that a minimum of 15 photons fell into each spectral bin. For the diffuse emission, the extraction circle (Fig. 2) was 40″ in diameter and centered 4″ to the northeast of the point source; events were grouped to a minimum of 20 counts per energy bin. To allow for consistency checks, two regions were used to estimate the contribution of background emission to the source spectra (see Fig. 1): an annular arc to the north of the nebula with inner and outer radii 2.1′ and 2.5′ respectively, centered on the point source and extending out to the chip gaps to its east and west; and a circular region (radius 1.2′) at the northern corner of the I3 chip, where there is essentially no radio emission from the

remnant.

Events contained within the point source region reflect an evidently soft-spectrum origin: in the energy band above 2.5 keV, the countrate is consistent with the surface brightness of the surrounding diffuse emission, so that the point source is cleanly detected only at low energies. Blackbody spectral models adequately describe this emission, with best-fit parameter values that do not depend, to within estimation uncertainties, on which background region is used. In the diffuse emission, there were too few counts to allow for quantitative analysis of any features or sub-regions other than the integrated nebula, which exhibits a hard tail consistent with an absorbed power-law spectral model.

Statistically, the most well-constrained spectral fits were those made for the point-source (blackbody) and diffuse (power-law) emissions simultaneously, with a common interstellar absorption parameter, the neutral hydrogen column density $N_{\rm H}$. We verified that fits to each component separately produced consistent results, finding however that poor statistics prevented measurement of $N_{\rm H}$ in either fit alone—even in the simultaneous analysis, the best-fit value $N_{\rm H} = (0.23 \pm 0.17) \times 10^{22}$ cm^{-2} amounts to an upper limit at the 2σ level. Observed and model spectra derived from the simultaneous analysis are shown in Figure 4, together with confidence contours projected onto two-dimensional slices of the full five-dimensional parameter grid. Least squares minimization produced the best fit at a reduced $\chi^2 \simeq 0.5$ for 27 degrees of freedom.

For the point source, power-law fits were formally acceptable (reduced $\chi^2 \simeq 0.7$), but produced steep spectra (photon indices $\Gamma \sim 3.5$) when $N_{\rm H}$ was fixed at the nebular value, and steeper still when $N_{\rm H}$ was allowed to vary up to five times the nebular value. We prefer instead thermal models: a blackbody spectrum yields a best-fit temperature of $0.23^{+0.06}_{-0.04}$ keV (uncertainties are 1σ throughout), for a bolometric unabsorbed flux of $\sim 8 \times 10^{-14}$ ergs cm^{-2} s^{-1}. The isotropic luminosity of the source is then

$L_X \sim 10^{31}\,(d/1\ \mathrm{kpc})^2$ ergs s^{-1} for distance d, implying for a simple blackbody an emitting area with a characteristic radius of $\sim 0.3\,(d/1\ \mathrm{kpc})$ km. This size is consistent with the area of a magnetic polar cap, heated by bombardment of particles accelerated in the magnetosphere, on a neutron star surface. Propagation effects in stellar atmospheres, however, are believed to significantly distort thermal spectra, making temperature and size estimates unreliable, with pure blackbody fits tending to overestimate temperatures by up to a factor of two depending on the magnetic field strength and composition of the atmosphere.

To investigate the possible impact of an atmosphere, we used the `XSPEC` NSA model (Pavlov et al. 1995, Zavlin et al. 1996) to fit the point-source spectrum to presumed emission from the entire stellar surface for nonmagnetic atmospheres as well as $B = 10^{12}$ and 10^{13} G conditions. For canonical neutron star mass (1.4 $M_\odot$) and radius (10 km) assumptions, these fits also provide a distance estimate, as the emitting area seen by a distant observer is fixed. The fits demonstrated that reasonable values of effective surface temperature and distance (shown in Table 1; their implications are discussed in Sec. 4.1) could be inferred from the available data, but we found that the NSA model parameters, effective temperature and overall normalization, were highly covariant with one another in every case, with the χ^2 surface describing an extended, shallow minimum, precluding a well-bounded measurement of either quantity by itself. The implied luminosity, which depends on both temperature and the normalization, is more reliably constrained. These ill-defined fits were likely the result of poor statistics and the necessarily coarse binning of our observed spectrum; we note, however, that the number of fitting parameters was the same whether we used the NSA models or a simple blackbody, where the latter produced much more robust parameter estimations. Also unlike the blackbody model, the NSA fits all required a hydrogen absorbing column N_{H} some three times higher than is supported by our preferred power-law fit to the nebular emission surrounding the point source, as

described below. When fit simultaneously, $N_{\rm H}$ remains high while the nebular spectrum exhibits unmodeled excess flux at energies $\lesssim 1$ keV. Attempts to model this excess with additional thermal or nonthermal spectral model components were inconclusive. A deeper observation will be needed to better constrain atmosphere fits and resolve the apparent inconsistency between absorbing columns for the point source and surrounding nebula.

For the nebula, the best-fit photon index is $\Gamma = 1.63 \pm 0.30$, for 0.5–10 keV and 2–10 keV unabsorbed fluxes of 2.8×10^{-13} and 1.8×10^{-13} ergs cm^{-2} s^{-1}, respectively. The implied 0.5–10 keV isotropic luminosity is $L_X \simeq 3.3 \times 10^{31}\ (d/1\ {\rm kpc})^2$ ergs s^{-1}. These results are largely in line with the *ASCA* measurements reported by ASLK04: the power-law photon index is virtually identical, but the source luminosity derived from *ASCA* data is a factor of 4 higher than the *Chandra* value. This discrepancy may be attributable to contamination from the point source and other, unrelated, sources, as well as incomplete background subtraction in the low-angular-resolution *ASCA*-GIS observation, although variability cannot be ruled out without further observations. The newly measured $N_{\rm H}$ is also consistent with the *ASCA*-derived value; at roughly one-sixth of the full Galactic column density, it supports prior evidence of a small distance to DA 495.

3.2.2. Constraints on nebular thermal emission

The only significant diffuse X-ray emission in our *Chandra* image is the nebula that lies within $\sim 40''$ of the point source, i.e., largely inside the radio "hole." Fitting this emission to thermal models yields statistically acceptable results—with, e.g., a bremsstrahlung temperature of 10 keV—but these temperatures are significantly higher than those typically seen in shock-heated supernova remnant interiors ($\lesssim 3$ keV). A thermal origin of the X-ray nebula is therefore disfavored. More importantly, in a "thick shell" interpretation of the radio emission as being thermal in nature, one would expect significant spatial

correspondence between thermal X-ray emission and the bright radio annulus. No X-ray emission in an annular or shell-like structure is seen.

To quantitatively constrain the X-ray flux from the regions coincident with the radio annulus, we defined an annular region with inner and outer radii of $1.7'$ and $5.5'$ respectively and centered on the radio hole, from which to extract source photons. Chip gaps were excluded, and unresolved sources detected by the `vpdetect` tool were removed. To estimate the local background, we defined two regions (as a check on the consistency of the results), one at the northern corner of the I3 chip, and another taking up most of the S2 chip (cf. Fig. 1). The countrates in both of these detector regions were degraded by $\simeq 15\%$ due to mirror vignetting, resulting in an overestimate of the source flux in a background-subtracted analysis. For the purpose of setting a conservative upper limit on the source flux, however, this is acceptable. We find that the maximum allowable count rate in a diffuse component within the radio-bright annulus is 0.048 cts s^{-1} (3σ) in the 0.5–5 keV band, for a surface brightness $< 10^{-3}$ cts $pixel^{-2}$; corrected for vignetting, the upper limits on photon flux are 9.5×10^{-5} cts cm^{-2} s^{-1} and 9.4×10^{-11} cts cm^{-2} $pixel^{-2}$.

3.3. Timing Analysis

The photon time tagging resolution provided by the Chandra CCDs in full imaging mode is 3.2 s, much too poor to allow for a periodicity search for a typical young, rotation-powered pulsar. We did, however, attempt to confirm the putative 10.9 s pulse period we identified, with low statistical significance, in the *ASCA*-GIS data (ASLK04). In Fourier and Bayesian epoch-folding (Gregory & Loredo 1992) analyses, we detected no flux modulations at that, or any other, pulse period $\gtrsim 10$ s, nor was there any evidence of flaring or other variability in the point source and nebular fluxes.

4. Discussion

4.1. Thermal properties of the point source and nebula

For the putative pulsar powering the DA 495 nebula, power-law spectral fits are statistically acceptable but yield uncomfortably large photon indices and much larger absorption columns than are supported by the spectral fits to the nebula. For nominal fits to the NSA atmosphere models, the bolometric luminosity for an assumed age may be compared with neutron star cooling curves from theory and the blackbody temperatures and luminosities of other pulsars with similar ages (Tsuruta et al. 2002). KLR+07 estimate the age of DA 495 at 20 kyr. For this assumed age, the putative neutron star in DA 495 is underluminous by a factor 5–10 compared with expectations from standard cooling models, $L_X \sim 10^{33}$ erg s^{-1}, assuming the NSA fit results are reliable. For the blackbody fits, the implied area and temperature are not unreasonable for emission from a heated polar cap, but if the observed flux is dominated by polar caps, the contribution from cooling over the remaining surface would have to be $\lesssim 10^{29}$ erg s^{-1}, 3–4 orders of magnitude lower than cooling theories can accomodate.

The absence of detectable diffuse thermal emission, either on large scales or as in 3C58 where thermal and nonthermal emission are mixed (Gotthelf et al. 2007), suggests two possibilities. Either no reverse shock has developed, and therefore the PWN is expanding into cool surroudings (presumably ejecta), as in the Crab, or emissions driven by the reverse shock have already dissipated. That a reverse shock, in the former scenario, has not yet produced significant heating of ejecta nor interacted with the PWN in a $\sim$ 20 kyr-old remnant would be somewhat surprising, but the absence of a detectable limb-brightened shell surrounding DA 495 may be significant—the existence of a forward shock is a prerequisite for the formation of a reverse shock. In the second case, i.e., in which the hot ejecta that signal the passing of a reverse shock have already cooled and dissipated,

interaction with a reverse shock would be expected to compress and distort a PWN (van der Swaluw et al. 2001, Blondin et al. 2001); for high-velocity pulsars, spatial offsets between the radio and X-ray emissions may result as in, e.g., SNR G327.1−1.1 (Gaensler & Slane 2006). Compression of the DA 495 X-ray PWN, which is dominated by current-epoch energy input from the neutron star, is plausible given its size relative to the radio PWN, which reflects the star's luminosity soon after birth. There is, however, no measurable offset between the radio and X-ray emissions for DA 495, both appearing to be tied to the current pulsar position to within the $\sim 15''$ angular resolution of the available radio images, suggesting a low velocity. In any case, a thermal origin for the radio emission is virtually ruled out; KLR+07 provide further arguments against such a "thick shell" interpretation.

4.2. Termination shock

Pulsar wind nebulae are synchrotron structures that depend on the perturbation of free-flowing particles at a standing shock. Of immediate interest in an observed nebula, then, is whether the termination shock has been detected. Regardless of whether the wind is confined by ram pressure induced by the pulsar's motion or simply ambient pressure in a medium, the shock is typically seen as the transition from an underluminous (free-flowing) zone to a brighter region. The only feature in our *Chandra* image of DA 495 that approximately matches this description is the "hook" near the central point source: there is a hint of a deficit of X-ray flux where the "hook" curves southward. If significant, this may represent the inner shock front where the pulsar wind is equatorially confined; if the apparent deficit is a statistical fluctuation, however, the rest of the nebula, consistent with post-shock emission, suggests that the inner shock is unresolved. We therefore assume an upper limit on the shock radius, consistent with the extent of the hook, of $4''$, or $r_s \lesssim 0.02\,(d/1\ \mathrm{kpc})$ pc.

Given this radius, we can set a limit on the spin-down luminosity of the pulsar, $\dot{E} \lesssim 4\pi c r_s^2 P_{\rm PWN}$, through the nebular pressure, $P_{\rm PWN}$. The latter can be estimated from the radio-derived equipartition magnetic field in the PWN of 1.3 mG (KLR+07; see below) so that $P_{\rm PWN} \simeq 1.3 \times 10^{-7}$ dyn cm^{-2}. The resulting upper limit on $\dot{E}$ is 2×10^{38} ergs s^{-1}. An independent estimate of $\dot{E}$ is available by assuming a Vela PWN-like efficiency of conversion from spin-down to nebular luminosity, $L_X/\dot{E} \simeq 10^{-4}$ (Pavlov et al. 2001), which, given the power-law luminosity we derive above, implies $\dot{E} \sim 5 \times 10^{35}$ ergs s^{-1}, nearly three orders of magnitude below the value implied by the putative termination shock radius, a result that suggests the true shock offset from the point source is likely to be unresolvable ($\simeq 0.1''$) if the spin-down luminosity is indeed small. Otherwise, the nebular conversion efficiency would have to be $\sim 10^{-7}$.

If the hook is not part of the termination shock, it belongs among the family of compact X-ray features seen in the close vicinities of pulsars powering wind nebulae, most of which are poorly understood. Gaensler et al. (2002) describe several such post-shock features for PSR B1509−58, including apparent toroidal wisps analogous to those seen in the equatorial outflow from the Crab. The DA 495 hook may be the visible portion of a similar wisp, arising either from thermal instabilities due to synchrotron cooling (Hester 1998) or compression of particle pairs by magnetic reflections of heavy ions (Gallant & Arons 1994).

4.3. Morphology and connection to radio properties

That the pulsar wind in DA 495 is confined by ambient rather than ram pressure is supported by two observations: (1) the X-ray PWN morphology does not resemble a bow shock or narrow "trail" of emission (cf. PSR B1957+20; Stappers et al. 2003), and (2) despite the spatial offset of the point source from the center of the radio annulus, a low

velocity—at most a few tens of km s^{-1}—is suggested by the anchoring of the polarized radio emission (which is due to long-lived particles injected soon after the pulsar was born) at the current position of the pulsar (KLR+07). The radio hole, then, may plausibly be attributed to an absence of synchrotron-emitting particles in a region similar to the so-called optical "bays" seen in the Crab nebula (Fesen et al. 1992). Regrettably, the spacecraft roll angle during the observation was such that the coordinates of the radio hole largely fell upon one of the chip gaps in the ACIS-I array (Fig. 1), resulting in poor sensitivity to any X-rays from the hole region.

The only feature in the X-ray PWN that hints at axisymmetry is the putative NE extension. Even though its existence depends on only a dozen or so detected photons in our *Chandra* image, the orientation (projected on the sky) provided by three independent measurements (radio, *ASCA*, *Chandra*) suggests consistency with the morphologies of many other PWNs, including the Crab and that around PSR B1509−58 (Gaensler et al. 2002), the greatest spatial extents of which lie along their pulsar spin axis directions. Two mechanisms generally explain the elongated shapes[2]: the lower confining pressure along the pulsar's spin axis produces a larger termination radius than does the high-pressure toroidal field in the equatorial direction, and the weaker nebular magnetic field along the spin axis results in longer post-shock synchrotron lifetimes. The latter is probably the correct explanation for the NE extension, if real, in DA 495, given the likelihood that its termination shock is unresolved.

Aside from orientation, the radio model of KLR+07 provides a further bit of evidence in support of the NE extension in DA 495: the radio polarization-derived inclination of

[2]The elongations and extensions referred to here are distinct from the narrow, collimated "jet" outflows also seen in several of the same PWNs and aligned with the pulsar spin axes—we find no evidence for such a jet in our X-ray images of DA 495.

the magnetic field vector to the line of sight, $\sim 55°$, shows the field pointing away from us to the SW, so that the *Chandra* brightening to the NE (and perhaps much of the overall E-W asymmetry in X-ray flux) is consistent with Doppler boosting, especially given the relativistic flow speeds implied by the synchrotron cooling time (see below). In the unlikely event that the "hook" to the east and south represents a portion of the wind termination shock, then the DA 495 X-ray structure would be reminiscent of the PWN in G54.1+0.3 (Lu et al. 2002) and other objects (e.g., Ng & Romani 2004) in that both the equatorial and polar (jets, in most cases) structures, ostensibly orthogonal to one another, are brightened on the same side of the pulsar, a situation difficult to reconcile entirely with Doppler boosting. This is perhaps a further point against identification of the hook with the termination shock.

Comparison of the radio and X-ray spectra is also instructive. KLR+07 find that the broadband radio spectrum of DA 495 shows a break near 1.3 GHz; arguing that this break is due to synchrotron cooling, rather than an injected break (i.e., one intrinsic to the spectra of radiating particles), they use the break frequency to estimate a nebular magnetic field strength of 1.3 mG. The measured spectral slopes below and above the break are $\alpha_{\rm Rlo} = -0.45 \pm 0.2$ and $\alpha_{\rm Rhi} = -0.87 \pm 0.1$ respectively. The bulk of the radio emission is due to particles that were injected into the nebula/soon after the pulsar was born, when spin-down luminosity was at its peak. Particles emitting at frequencies below the present-day break have nonetheless not radiated away a substantial portion of their energy. In contrast, the X-ray emission is dominated by particles that have only recently been injected (see below). If the assumed cooling origin of the break is correct, if the injected particle spectrum is unbroken between the radio and X-ray bands, and finally if the injected spectrum has not changed substantially since the pulsar was born (despite declining in particle luminosity) then one expects that the X-ray spectral slope $1 - \Gamma$ should lie somewhere between the two radio spectral slopes, and perhaps closer to $\alpha_{\rm Rlo}$.

This is indeed observed, although hardly conclusively: numerically, the X-ray power-law photon index $\Gamma = 1.63$ is consistent with both of the radio spectral indices given the rather large combined uncertainties. Still, the assumptions above appear not to be violated and, moreover, any injected break at an intermediate frequency between radio and X-ray, such as those seen at tens of GHz in three filled-center SNRs (G29.7−0.3, 3C58, and G16.7+0.1; see KLR+07) must be weak.

Because of the short exposure and low surface brightness of the DA 495 X-ray nebula, it was not possible to search for spectral steepening with radial distance from the pulsar, but the vastly different sizes of the X-ray and radio nebulae suggest that synchrotron cooling is very efficient, consistent with the high magnetic field value derived by KLR+07.

4.4. Wind magnetization

The synchrotron lifetime of particles emitting at energy ϵ keV in a magnetic field B in μG is $\tau_{\rm synch} = 39 B^{-3/2} \epsilon^{-1/2}$ kyr. For the radio-derived field strength of $B = 1.3$ mG and emission at $\epsilon = 1.5$ keV, the radiating lifetime is $\tau_{\rm synch} = 0.68$ yr. Thus, the DA 495 PWN imaged with *Chandra* is dominated by particles less than one year old. The velocity necessary to traverse the roughly 20″, or $0.1\,(d/1\ {\rm kpc})$ pc, radius of the nebula in 1 yr is $0.33c$. Lu et al. (2002) similarly find a velocity a substantial fraction of c for the G54.1+0.3 PWN in the flow immediately downstream of the termination shock; in the case of DA 495, however, the termination shock at radius r_s is apparently unresolved and the ratio of r_s to the PWN radius is at most 0.1, so that the relativistic flow must extend to a great distance post-shock. Relativistic bulk velocity at a large downstream distance has also been inferred for a linear feature in the N157B PWN (Chen et al. 2006), but is thought to arise from strong pressure confinement due to a nearby dense cloud. For DA 495, the work of Kennel & Coroniti (1984) suggests that relativistic bulk motion at large radii is only possible for

values of the "magnetization parameter," the ratio of electromagnetic to particle energy flux in the pulsar wind, of $\sigma \simeq 0.4$. By contrast, for G54.1+0.3, $\sigma = 0.06$, while for the Crab it is smaller still, $\sigma = 0.003$. In fact, all estimates of σ to date have found that the observed PWNs are driven by strongly particle-dominated winds (Petre et al. 2007; e.g.,). For DA 495, the contributions of Poynting and particle flux appear to be nearly equal.

The conclusion that the pulsar wind in DA 495 has high magnetization seems difficult to avoid, as it is based on a reliable inferred nebular magnetic field and the observed size of the X-ray PWN. In fact, the radio B-field measurement applies to significantly larger radii than the extent of the X-ray PWN, so that the inner-nebula field may be stronger than we have assumed, further reducing radiating lifetimes and pushing the magnetization parameter to still higher values. Importantly, Kennel & Coroniti (1984) show that, naturally, particle dominated winds are necessary for efficient conversion of wind luminosity to synchrotron luminosity. Gotthelf (2004) has pointed out that pulsars with spin-down luminosity less than $\simeq 4 \times 10^{36}$ erg s^{-1} host substantially dimmer PWNs than their more luminous counterparts. It is tempting to speculate that the magnetization fraction σ varies either with spin-down luminosity or, more likely, with time such that older, less luminous pulsars produce dim nebulae because their winds are Poynting-flux dominated. Current understanding of magnetospheric physics for rotation-powered pulsars argues for a strongly field-dominated wind at the light-cylinder, $\sigma_{\rm LC} \sim 10^4$. The very small measured values of σ imply conversion, through an unknown mechanism, to a strongly particle-dominated wind by the time the flow reaches the termination shock, at least for the youngest and most energetic pulsars. Phenomenologically, a scenario in which σ reverts to large values for older or less-luminous pulsars would imply a turning-off of the mysterious mechanism that brightens pulsar wind nebulae around Crab-like stars.

5. Conclusions

The soft spectrum of the unresolved source near the center of the DA 495 radio nebula, its implied blackbody temperature and luminosity, and its lack of variability on timescales of a few seconds through the 25 ks duration of the observation are highly suggestive of emission from the surface of an isolated neutron star. Taken together with the properties of the surrounding extended emission—entirely consistent with a pulsar wind nebula driven by the magnetosphere of a rotation-powered pulsar—little doubt remains that DA 495 is a pulsar-powered supernova remnant. Its unusual properties can be explained as the result of aging in the absence of any evident interaction with the supernova explosion's reverse shock, such that DA 495 presents a valuable example of a pristine PWN at an advanced age.

Support for this work was provided by the National Aeronautics and Space Administration through *Chandra* Award Number GO3-4092A issued by the *Chandra* X-ray Observatory Center, which is operated by the Smithsonian Astrophysical Observatory for and on behalf of the National Aeronautics and Space Administration under contract NAS8-03060. The CGPS is a Canadian project with international partners and is supported by the Natural Sciences and Engineering Research Council (NSERC).

REFERENCES

Arzoumanian, Z., Safi-Harb, S., Landecker, T. L., & Kothes, R. 2004, ApJ, 610, L101

Blondin, J. M., Chevalier, R. A., & Frierson, D. M. 2001, ApJ, 563, 806

Chen, Y., Wang, Q. D., Gotthelf, E. V., Jiang, B., Chu, Y.-H., & Gruendl, R. 2006, ApJ, 651, 237

Fesen, R. A., Martin, C. L., & Shull, J. M. 1992, ApJ, 399, 599

Fruscione, A., McDowell, J. C., Allen, G. E., Brickhouse, N. S., Burke, D. J., Davis, J. E., Durham, N., Elvis, M., Galle, E. C., Harris, D. E., Huenemoerder, D. P., Houck, J. C., Ishibashi, B., Karovska, M., Nicastro, F., Noble, M. S., Nowak, M. A., Primini, F. A., Siemiginowska, A., Smith, R. K., & Wise, M. 2006, in Observatory Operations: Strategies, Processes, and Systems. Edited by Silva, David R.; Doxsey, Rodger E.. Proceedings of the SPIE, Volume 6270, pp. 62701V (2006).

Gaensler, B. M., Arons, J., Kaspi, V. M., Pivovaroff, M. J., Kawai, N., & Tamura, K. 2002, ApJ, 569, 878

Gaensler, B. M. & Slane, P. O. 2006, ARA&A, 44, 17

Gallant, Y. A. & Arons, J. 1994, ApJ, 435, 230

Gotthelf, E. V. 2004, in Bulletin of the American Astronomical Society, Vol. 36, Bulletin of the American Astronomical Society, 917–+

Gotthelf, E. V., Helfand, D. J., & Newburgh, L. 2007, ApJ, 654, 267

Gregory, P. C. & Loredo, T. J. 1992, ApJ, 398, 146

Hester, J. J. 1998, Memorie della Societa Astronomica Italiana, 69, 883

Kennel, C. F. & Coroniti, F. V. 1984, ApJ, 283, 694

Kothes, R., Landecker, T. L., Reich, W., Safi-Harb, S., & Arzoumanian, Z. 2007, ApJ, submitted

Landecker, T. L. & Caswell, J. L. 1983, AJ, 88, 1810

Lu, F. J., Wang, Q. D., Aschenbach, B., Durouchoux, P., & Song, L. M. 2002, ApJ, 568, L49

Mori, K., Tsunemi, H., Miyata, E., Baluta, C. J., Burrows, D. N., Garmire, G. P., & Chartas, G. 2001, in ASP Conf. Ser. 251: New Century of X-ray Astronomy, ed. H. Inoue & H. Kunieda, 576–+

Ng, C.-Y. & Romani, R. W. 2004, ApJ, 601, 479

Pavlov, G. G., Kargaltsev, O. Y., Sanwal, D., & Garmire, G. P. 2001, ApJ, 554, L189

Pavlov, G. G., Shibanov, Y. A., Zavlin, V. E., & Meyer, R. D. 1995, in The Lives of the Neutron Stars. Proceedings of the NATO Advanced Study Institute on the Lives of the Neutron Stars, held in Kemer, Turkey, August 29-September 12, 1993. Editor(s), M.A. Alpar, U. Kiziloglu, J. van Paradijs; Publisher, Kluwer Academic, Dordrecht, The Netherlands, Boston, Massachusetts, 1995. LC #: QB843.N4 L583 1993. ISBN #: 0-7923-324-6-6., p.71, ed. M. A. Alpar, U. Kiziloglu, & J. van Paradijs, 71–+

Petre, R., Hwang, U., Holt, S. S., Safi-Harb, S., & Williams, R. M. 2007, ApJ, 662, 988

Stappers, B. W., Gaensler, B. M., Kaspi, V. M., van der Klis, M., & Lewin, W. H. G. 2003, Science, 299, 1372

Tsuruta, S., Teter, M. A., Takatsuka, T., Tatsumi, T., & Tamagaki, R. 2002, ApJ, 571, L143

van der Swaluw, E., Achterberg, A., Gallant, Y. A., & Tóth, G. 2001, A&A, 380, 309

Velusamy, T., Becker, R. H., Goss, W. M., & Helfand, D. J. 1989, Journal of Astrophysics and Astronomy, 10, 161

Weisskopf, M. C., Hester, J. J., Tennant, A. F., Elsner, R. F., Schulz, N. S., Marshall, H. L., Karovska, M., Nichols, J. S., Swartz, D. A., Kolodziejczak, J. J., & O'Dell, S. L. 2000, ApJ, 536, L81

Zavlin, V. E., Pavlov, G. G., & Shibanov, Y. A. 1996, A&A, 315, 141

Table 1. Spectral fitting results for X-ray features in DA 495

Emission feature	Model	$N_{\rm H}$ (10^{21} cm^{-2})	$\log(T_{\rm eff})$ [K]	Γ	χ^2/ν	Dist. (kpc)	$\log(L_X)$ [erg s^{-1}]
Pt. source	BB	2.7 ± 2.0	6.40 ± 0.10	...	4.4/7	...	31.0
	H (0 G)	6.4 ± 0.7	~ 5.8	...	5.2/7	0.8	31.7
	H (10^{12} G)	6.9 ± 0.9	~ 6.0	...	5.9/7	1.5	32.3
	H (10^{13} G)	6.8 ± 0.9	~ 6.0	...	5.1/7	1.4	32.3
Nebula	PL	1.9 ± 1.7	...	1.58 ± 0.32	8.4/19	...	31.4
Pt. source	BB	2.3 ± 1.7	6.42 ± 0.08	...	4.4/7	...	31.0
+ nebula	+ PL		...	1.63 ± 0.27	8.5/19	...	31.3
Pt. source	H (10^{13} G)	6.0 ± 0.7	~ 6.0	...	4.9/7	1.8	32.4
+ nebula	+ PL		...	2.10 ± 0.24	13.8/19	...	31.8

Note. — Models BB and PL refer to blackbody and power-law spectra, respectively. H refers to the hydrogen-atmosphere NSA models in `XSPEC` with magnetic field strengths B given in parentheses. Luminosities, which for thermal and nonthermal models are bolometric and in the 2–10 keV band, respectively, assume a distance of 1 kpc if the spectral model does not provide an independent estimate.

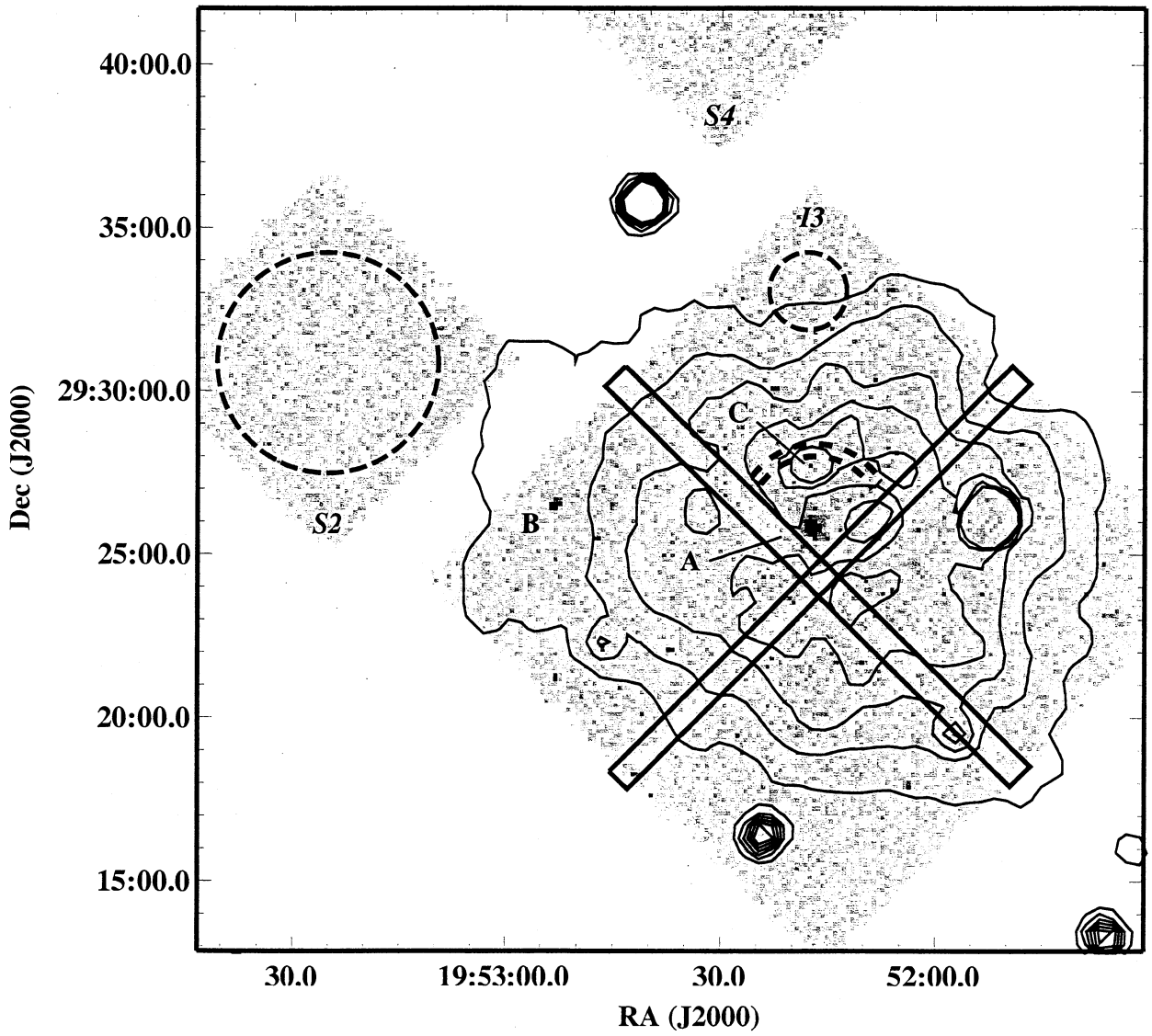

Fig. 1.— *Chandra*-ACIS image of the DA 495 field in a 25 ks exposure: X-ray counts in the 0.6–7 keV band, binned into 8″-pixels, are mapped on a logarithmic grayscale, with a maximum of 218 counts. Superposed contours show radio (1.4 GHz Canadian Galactic Plane Survey [CGPS]; see ASLK04) brightness temperatures between 1 and 6 K in 1 K steps. Three X-ray sources are labeled. Source A is the assumed pulsar and wind nebula near the center of DA 495. Source B is a Guide Star Catalog star previously detected by *ROSAT* (1WGA J1952.8+2926). Source C, newly designated CXOU J195217.3+292744, is apparently associated with an unresolved radio enhancement to the north of source A. Event extraction regions used for spectral background estimates are depicted by dashed circles and

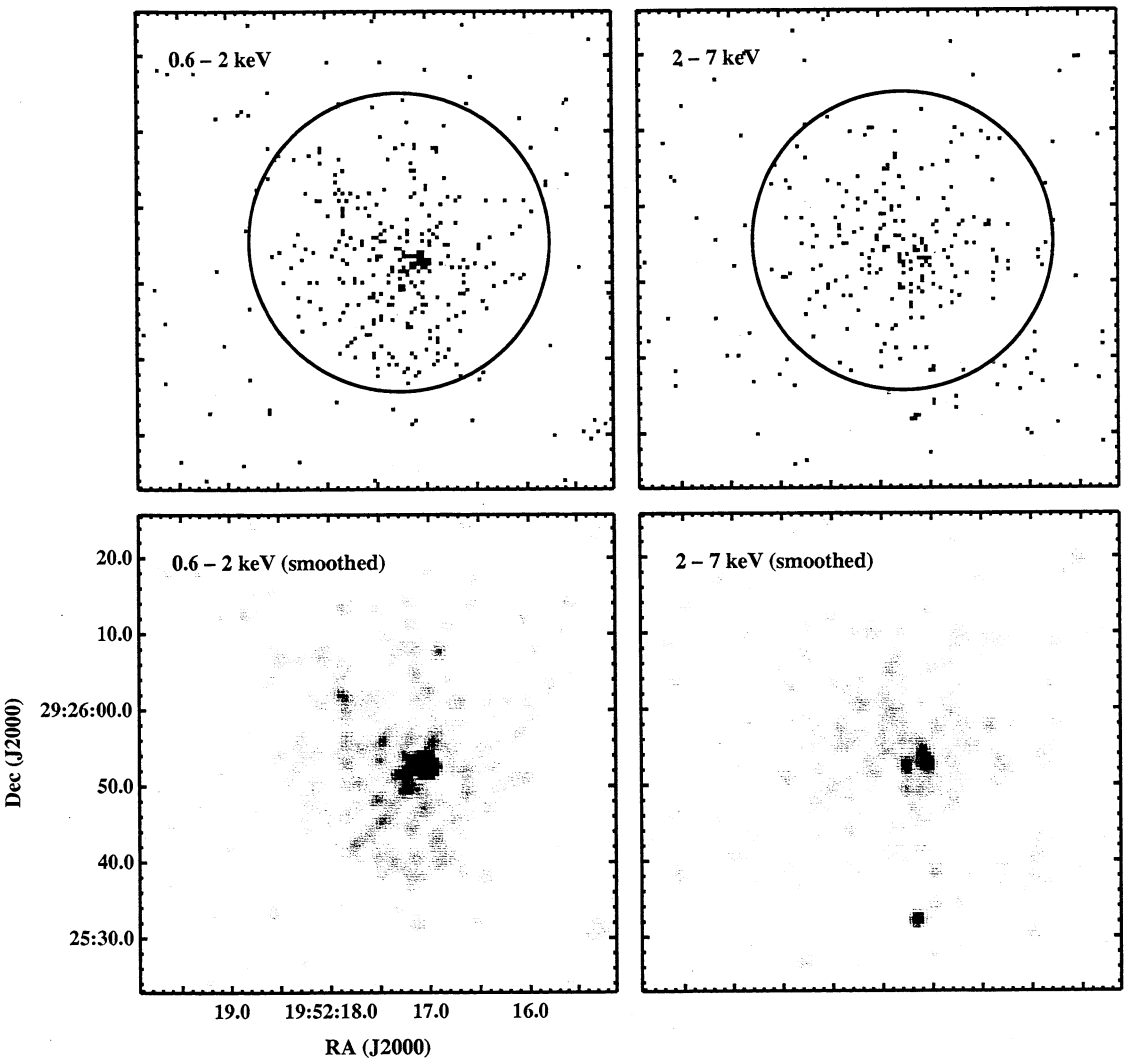

Fig. 2.— *Chandra* images of the central X-ray source in DA 495. *Upper panels:* Raw counts in two energy bands. The grayscale is logarithmic, with a maximum of 50 counts for the central pixel of the unresolved source in the 0.6–2 keV image. Solid circles depict the extraction region for spectral analysis of the nebula; for clarity, the 2″-radius extraction region centered on the point source is not shown. *Lower panels:* The same images smoothed by convolving with a Gaussian of width $\sigma = 3$ pixels. The grayscale is linear, truncated at 0.6 counts pixel^{-2}.

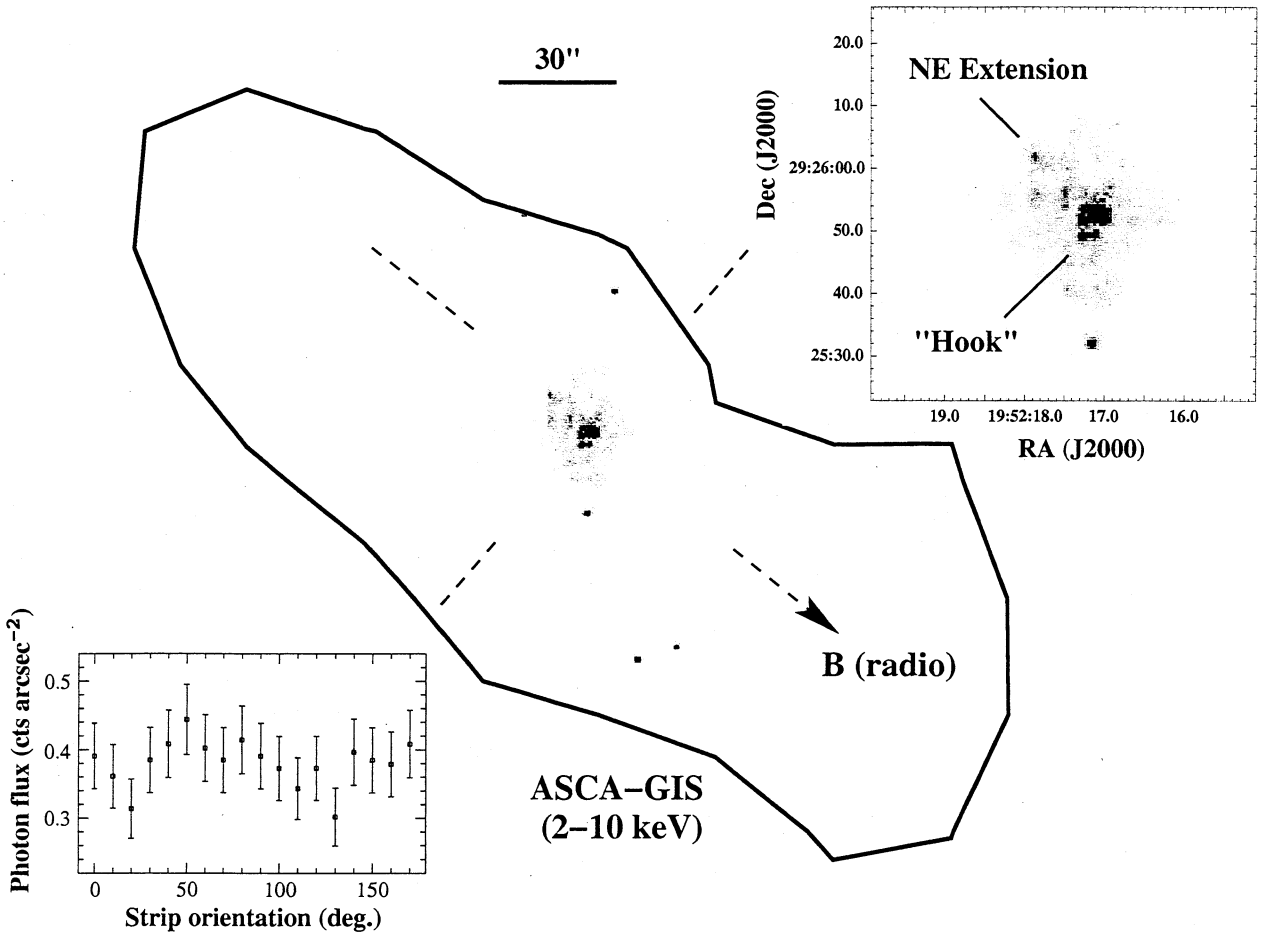

Fig. 3.— Adaptively smoothed 0.6–7 keV *Chandra* image in the context of an earlier *ASCA* observation and the magnetic field orientation derived from radio polarization measurements. The single heavy contour depicts the 0.75 counts pixel^{-2} level in the smoothed *ASCA*-GIS image (see Arzoumanian et al. 2004 for details). The dashed lines show the polar (*arrow*) and equatorial directions of the dipole field, on the plane of the sky, inferred from the radio rotation measure (Kothes et al. 2007). *Inset, upper right:* Close-up of the smoothed *Chandra* image, where a circular convolution kernel of varying size, requiring a minimum of 5 counts within the kernel diameter, has been applied. The greyscale is linear, truncated at 1 count pixel^{-2}. *Inset, lower left:* Summed counts within a rectangular extraction region 5 pixels wide and 150 pixels long, centered on the point source but excluding it, as a function of its orientation angle north through east.

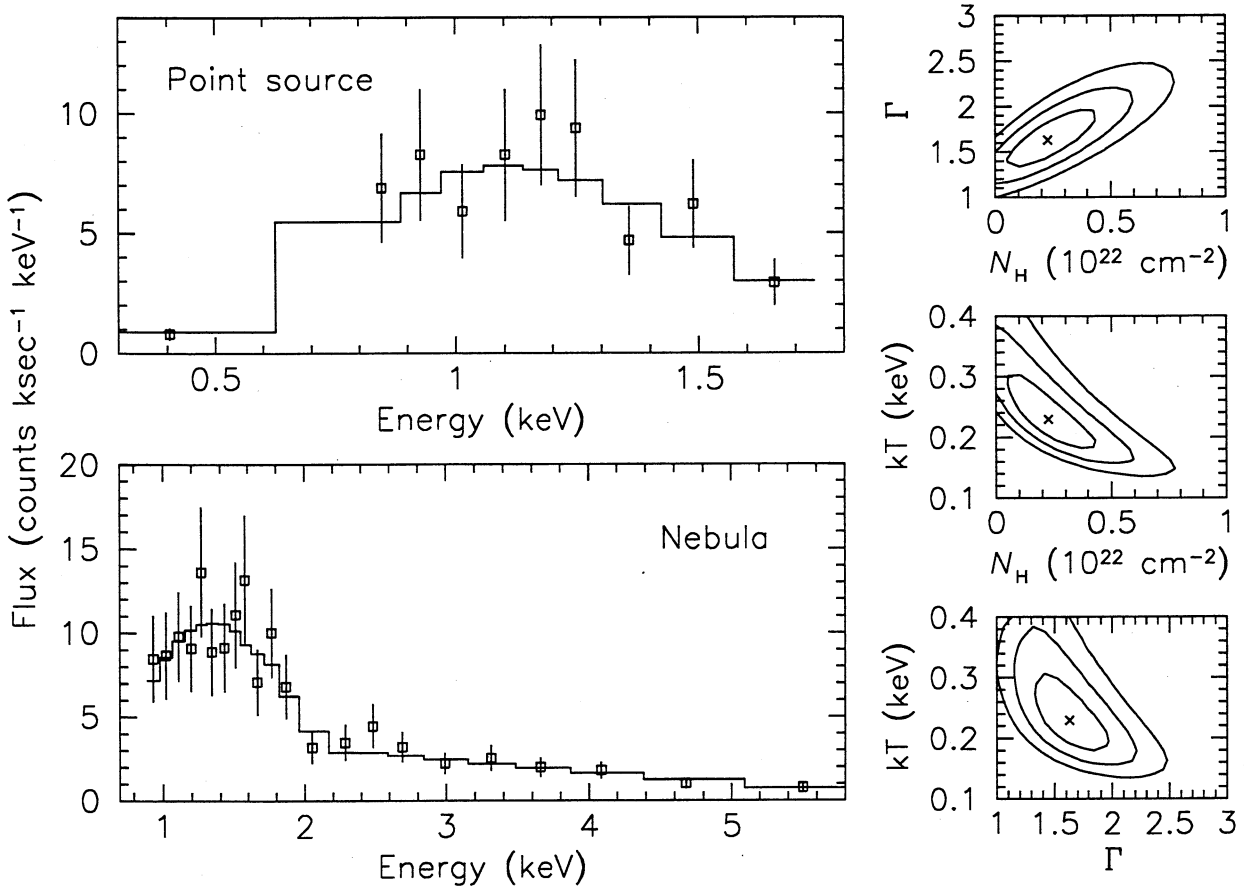

Fig. 4.— Photon flux spectra of the unresolved X-ray source (*top left panel*) and surrounding nebula (*bottom left*), fit simultaneously to blackbody and power-law models respectively, with a common neutral-hydrogen absorption ($N_{\rm H}$) parameter. To the right, projections of χ^2 in three planes of interest are plotted as contours representing 1, 2, and 3σ uncertainties in the parameter values, where kT is the blackbody temperature of the point source and Γ is the photon index of the nebula's power-law spectrum.